# **Experimental protocol for validation of Computational Fluid Dynamics palaeoecological simulations**

# Harriet B. Drage<sup>1</sup>, Stephen Pates<sup>2,3,4,5</sup> and Nicholas J. Minter<sup>6</sup>

# **Abstract**

Computational Fluid Dynamics (CFD) simulations are being used with increasing frequency to test palaeoecological hypotheses. These analyses output simulated velocity and pressure flow profiles, and drag and lift force values acting on a shape, for a given model of laminar or turbulent flow. These outputs are internally consistent, assuming consistently applied parameters. However, many simulations lack validation at the flow speeds and animal sizes modelled, and so the margins of error remain unquantified. Without certainty in the simulated outputs, we risk the resulting palaeoecological hypotheses lacking robustness. Experimental Fluid Dynamics (EFD) analyses using flume tanks can be performed to validate simulated force values, though these have rarely been done for palaeobiological research or at Reynolds numbers reflecting flow speeds and object sizes suitable for extinct invertebrates. We present work to produce a broadly applicable protocol for performing EFD analyses to generate drag and lift forces under different flow regimes, and velocity profiles. We discuss digital and print model production trade-offs, and present the lowcost, open-source force-measuring circuitry used. We test this EFD set-up by carrying out experiments on spheres, which we then compare to theoretical drag calculations. We also present the results of several experiments on animal models, comparing the results to comparable published CFD simulations. Sphere results track expected drag force and coefficient trends reasonably well, though are too low in magnitude. Experimental drag for an ammonite model almost exactly replicated data reported from CFD simulations, though other animal models differed due to experimental conditions. We discuss planned future refinement steps, following which a series of validation values will be produced for early Palaeozoic invertebrate body plans under different flow regimes in varied positions. These values can be used to validate CFD results of future studies, and the protocol replicated to support others in performing EFD validation of palaeoecological hypothesis-testing experiments.

<sup>&</sup>lt;sup>1</sup>Institute of Earth Sciences, University of Lausanne, Switzerland; harriet.drage@unil.ch

<sup>&</sup>lt;sup>2</sup>Department of Earth Sciences, University College London, UK; s.pates@ucl.ac.uk

<sup>&</sup>lt;sup>3</sup>Centre for Life's Origins and Evolution, Department of Genetics, Evolution and Environment, University College London, UK

<sup>&</sup>lt;sup>4</sup>Centre for Ecology & Conservation, University of Exeter, Penryn Campus, UK

<sup>&</sup>lt;sup>5</sup>Department of Zoology, University of Cambridge, UK

<sup>&</sup>lt;sup>6</sup>School of the Environment and Life Sciences, University of Portsmouth, UK; nic.minter@port.ac.uk

**Key words:** invertebrate, drag force, lift force, experimental validation, flume tank, fluid dynamics, palaeoecology, ultrasonic Doppler velocity

## Introduction

Computational Fluid Dynamics (CFD) methods are becoming more frequently employed to quantitatively test palaeoecological hypotheses for extinct animals, including how they moved, how they fed, and where they lived in the water column. Amongst others, CFD analyses on invertebrates have been used to test assumptions about feeding behaviours (e.g., in arthropods, Bicknell et al., 2021, 2023; in echinoderms, Rahman et al., 2015, 2020), locomotory hypotheses (e.g., in trilobites, Trenchard et al., 2017; Esteve et al., 2021; Song et al. 2021; Esteve & López-Pachón, 2023; *Isoxys* arthropods, Pates et al., 2021, 2024; archaeostracan arthropods, Pates & Xue, 2024), gill function (Hou et al., 2023), the life orientations of sessile organisms (e.g., Liu et al., 2022), and general shape hydrodynamic adaptations (e.g., Hebdon et al., 2020; Pates & Drage 2024; Pates et al., 2024). CFD simulates fluid flow around an object, such as a 2D or 3D animal model, and can be used to produce visual representations of velocity and pressure profiles, as well as estimated values of the drag and lift forces exerted on the object by the fluid (Rahman, 2017). These simulated results are then used to determine whether the hypothetical ecological modes are feasible, given particular model inputs, or how different morphological features would perform hydrodynamically in different fluid contexts (Rahman, 2017). The methods and application of CFD to palaeobiological research have been usefully reviewed by Rahman (2017), Gibson et al. (2020), and Gutarra & Rahman (2022).

Robust assessment of palaeoecological hypotheses therefore rests upon the validity of these simulated forces and profiles. However, while these are internally consistent (assuming consistently applied analytical protocol and parameters), the absolute values, and even magnitudes, of these forces often lack validation with empirical data. This is further complicated by the frequent extremely low values of these forces, due to the slow fluid flow regimes presumed for Earth's past (and present) large water bodies and the small sizes of many invertebrates, which means that validation experiments for more traditional engineering applications for CFD around larger objects and faster flow speeds cannot be used. The Reynolds numbers for flows around invertebrates (a measure predicting fluid flow patterns; Equation 1) are generally very low, which can complicate fluid flow simulations (e.g., Rauen et al. 2008; Li & Nielsen 2011).

$$Re = \frac{u L}{v} = \frac{\rho u L}{\mu}$$

where Re = Reynolds number; u = flow speed (m/s); L = characteristic linear dimension (m); v = kinematic viscosity of fluid (m<sup>2</sup>/s);  $\rho$  = density of fluid (kg/m<sup>3</sup>);  $\mu$  = dynamic viscosity of fluid (kg/(m·s)).

Equation 1

To date, very few studies have attempted experimental validation of their CFD analyses. Several studies, prior to the first application of CFD in palaeobiology, investigated the impacts of hydrodynamics (or

aerodynamics) on palaeobiology, palaeoecology and fossil preservation, though these are not usually directly comparable to present-day CFD simulations. For example, Hesselbo (1987) and Lask (1993) analysed the settling of trilobite sclerites in water to investigate the preservation of fossil sclerite orientations. Fortey (1985) analysed the streamlining of putative pelagic trilobite forms and terrace ridges. Plotnick & Baumiller (1988) tested a potential hydrodynamic function (as a steering rudder) for the telson of pterygotid eurypterids. Jacobs et al. (1994) recorded forces acting on ammonoid models in flume tank experiments, and Miller (1972) and Pearson (2017) explored water filtering through trinucleimorph trilobite fringe pits, both of which are potentially comparable to future CFD outputs. Palmer (2011) constructed model pterosaur wings, testing their aerodynamism in wind tunnel experiments, and comparing them to aerofoils; these results may also be comparable to future CFD simulations. Other experimental studies analysed flow around echinoderm models to test a variety of functional morphological hypotheses (see summary in Rahman 2020). Several recent studies carried out experiments that provide limited comparison to CFD simulations. Li et al. (2022) tested the drag forces acting on a model of the Cambrian arthropod Ercaicunia multinodosa placed in a water tank on a moving rig, which could be compared to simulated drag forces, though they did not measure lift forces and used a high level of model scaling, meaning that the experiments were at a higher Reynolds number than E. multinodosa would have experienced in life. Gibson et al. (2023) compared their CFD simulation results to early wind tunnel EFD results by Balsam and Vogel (1973) to assess the robustness of their conclusions on archaeocyathid feeding hypotheses. While not analysing the palaeobiology of an extinct organism, Davis et al. (2019) carried out a more holistic study on extant horseshoe crabs, using Particle Image Velocimetry (PIV) to track flow around the horseshoe crab model in experiments and using this to validate fluid flow simulations. Dynowski et al. (2016) carried out a similar study, examining flow patterns around an extinct crinoid species using CFD and experimental validation with PIV. Rahman et al. (2015) also used PIV measurements of the flow around cinctan echinoderm models in a flume tank to validate CFD simulations, with Rahman and Lautenschlager (2016) further employing the same method.

It is imperative that more work is carried out on experimental validation of palaeobiological CFD simulations, to provide a robust foundation for palaeobiological inferences from simulations. We therefore aim to produce a protocol for Experimental Fluid Dynamics (EFD), an area of research to broadly validate the results of CFD simulations in palaeobiology. We present in detail the experimental methods we have developed to facilitate palaeobiological EFD studies, such that others will be able to replicate and build on them to perform their own experiments. We also discuss several improvements that we will be making to the protocol and equipment, in the light of validation tests comparing experiments on spheres to theoretical calculations. Lastly, we compare EFD results (both drag forces and velocity profiles at intervals behind the models) for several animal models to comparable CFD studies, to provide a preliminary evaluation of congruence between the two methods.

## Materials and methods

# **Model production**

Digital models of spheres and of extinct animals were created manually in software Blender or sourced from published literature or online repositories (see below for sources). All digital model files are available open access; see below for the sources of all models used, and Supplementary Figure 1 for images of the models used. Models were 3D printed using stereolithography (SLA), which uses UV light to cure polymer resin, and provides a balance between cost and precision for printed prototypes. We used the on-site printing facilities at the University of Portsmouth, UK, using Elegoo 8K photopolymer resin and a Bambu Lab P1P printer. The 3D printing of animal models is a balance between several considerations (which may be analysed through design for manufacturability [DFM] analysis during model production): the scaling of the model, where life-size is ideal so as not to have to scale experimental measurements or change the density of the fluid, but often this is too small to enable precise printing of morphological features; the thickness of the modelled walls (thin model walls leads to unstable or unprintable models); surface intricate features, such as textures, which may impact experiments but are increasingly difficult to model at smaller sizes; and inclusion of intricate morphological features, such as spines, which will also impact experiments but are difficult to model accurately and without breakage either during printing or removing the model from the printed support structures. Animal models were scaled to be the same sizes as the digital models used for published CFD analyses, to enable as direct as possible comparison between the two sets of results.

The protocol presented here does not require the printed models to have comparable density to a real-world organism, because the model is always fixed in position (to the rod; see below). However, if planned experiments do not wish to fix the model to a similar structure, or the experiments plan to test hypotheses that involve extensive model movement (e.g., the moment of overturning in flow), then model density would be an important consideration.

#### **Force measurements**

All circuitry equipment used to measure forces exerted by the flow on the model was created by SparkFun [sparkfun.com]. Lift and drag forces were each measured by one 100 g capacity compression mini straight bar load cell (TAL221), wired to a Qwiic Scale amplifier (NAU7802), which was then connected using Qwiic cables to a Quiic Mux Breakout board (TCA9548A) and this to an OpenLog Artemis open-source data logger. Load cells translate pressure into electrical signals, measuring the electrical resistance proportional to the strain applied to the load cell. The OpenLog Artemis was then connected via USB-C to a MacOS laptop running Arduino 1.8.18, with force data logging directly onto the Arduino Serial Logger; we took the range of force measurements evident during a ~20 s period (variation due to movement of the model in increasing flow speeds) and recorded the median force. SparkFun components are a good choice for palaeontological EFD studies because they are inexpensive, rely on open-source programming, and are accessible thanks to extensive online community support.

Load cells used were rated only to IP65 (dust-tight and protected from water from a nozzle), rather than being immersible for brief periods (IP67) or fully submersible (IP68). This therefore necessitated rigging of

the load cells above the water flow (see section Jig production). This reflects the current technological limits of force measurement capability; aluminium alloy load cells can measure at the low force values being exerted on small models in low flow but are not submersible (best waterproofing available on the market was IP66), while stainless steel is submersible but cannot measure force values low enough as it requires more force to deform.

## Velocity profile measurements

The velocity profile of the flow was measured using an ultrasonic Doppler velocity profiler (UDVP), a Nortek Vectrino Profiler Fixed Probe. We suspended the UDVP above the flume tank, with the arm of the UDVP placed in the water flow (Fig. 1). The arm is comprised of a beam and four receptors, capable of measuring the velocity of flow in the x, y, and z axes. The UDVP must be centred in the tank and positioned so that the arm is exactly vertical, perpendicular to the long axis of the tank, otherwise the measured velocity along the x axis of the tank will be recorded by the velocimeter as a combination of the x, y and z axes. The UDVP was set to measure along a vertical depth of 30 mm (the maximum), sampling the flow at every 1 mm depth, starting at a focal depth 40 mm from the tip of the probe. Most models had heights >30 mm, so we positioned the UDVP at heights such that this vertical measurement encompassed the vertical space across the majority of the model, with additional space either above or below the model (see Supplementary Data for the UDVP heights in each model test). This equates to 31 velocity points and 31 depth points being measured simultaneously at each timestamp the Vectrino was running, from 40–70 mm from the tip of the probe. The UDVP was connected to a laptop running Windows 11, and velocity measurements made using the proprietary Vectrino Profiler software (Nortek Multi-Instrument Data Acquisition System version 1.37.4428, not functional on MacOS) packaged with the UDVP. We moved the UDVP on a horizontal runner above the flume tank during each of the model tests such that we measured the velocity profile as close behind the model as possible, at distances behind the model that were intended to represent roughly between 2 and 10 diameters of the model (depending on the scaling of the model itself), and more than 10 diameters behind the model at which point the impact of the model on the flow will be much reduced or absent. For smaller models the size of the jig provided a physical constraint to placing the UDVP, and so the UDVP was placed as close behind the model as possible. Each distance measured from each model is given in Supplementary Data.

Data were recorded by the Vectrino Profiler software in proprietary .ntk format. These were converted to ASCII format using the same software using the 'export ASCII' function ('Data' dropdown menu). Periods of time where the flow was developing (e.g., during starting the flume or changing flow velocity) were excluded from the export. These ASCII files were then read into R, and manipulated in order to extract the x velocities, profile depths (distance from the sensor to the x velocity being measured; 31 in total at 1 mm intervals), bottom depths (distance from the sensor to the bottom of the tank), and time stamp for each measurement. These data were exported as a .csv file for further analysis and plotting in R. R code for these manipulations, raw .ntk files, and exported .csv files are provided in the Supplementary Code file. We use

'inlet velocity' to refer to the velocity of the water flow produced by the flume tank, that is, the velocity the water flows at past the inlet valve. We use 'profile velocity' to refer to the velocity of the water flow as measured by the Vectrino Profiler, with a series of measurements at set distances from the tip of the probe.

# Jig production

A jig to support the load cells the models was modelled as a Computer-Aided Design file, then built in the University of Portsmouth workshop out of acrylic (Fig. 1A–C) and the load cells glued onto the jig using epoxy resin. A 3 mm-diameter carbon fibre rod was used to attach the 3D-printed model to the jig. The rod can be unscrewed and connected at two different points in the jig, enabling force recording by either of the two load cells on the jig. One load cell is mounted with the compression force parallel to the rod movement direction to measure drag, and the other load cell is mounted perpendicular to this to measure lift.

The jig was then mounted to the rails above an Armfield S6 linear flume tank at the University of Portsmouth using g-clamps (Fig. 1). The model was mounted on the end of the rod in the flume and the other end of the rod screwed into the jig. We used rods of just under 50 cm, which positioned the model approximately in the vertical middle of the flow of water within the flume tank.

# **Experiments**

With the model mounted on the rod in the flume tank, attached to the jig with load cells logging force data, and the UDVP mounted and measuring the velocity profile behind the model, the water flow in the flume tank was then turned on (Fig. 1D). We adjusted the water inflow rate and height of the outflow ramp while maintaining the water height at 30 cm to attain five flow velocities (0 m/s, 0.05 m/s, 0.1 m/s, 0.2 m/s, and 0.3 m/s). We then measured drag forces acting on the model, and multiple velocity profiles at different distances behind each model, for each of the flow velocities by sequentially increasing the water inflow rate and lowering the outflow ramp to raise the velocity whilst maintaining a flow depth of 30 cm. After this, we demounted the model, affixed it to the lift load cell, and measured lift force across the same flow velocities, using the UDVP to confirm these flow velocities at each point. Only flow velocities 0.05–0.3 m/s were possible to test in the Armfield S6 flume tank; at higher velocities the water level in the tank dropped below 30 cm and a wave developed on the surface of the flow. We measured the range of force values over 20 s for both drag and lift observations, then used the median observed force for all subsequent calibrations and analyses.

We tested the experimental set-up and protocol using 3D-printed spheres with diameters 10 mm, 25 mm, 50 mm and 75 mm. In addition, we 3D-printed three animal models that are comparable to those previously used for published CFD studies to compare the EFD results to simulated force data. For this study, we tested models of the horseshoe crab *Limulus polyphemus* (open-source 3D-scan by Thingiverse user GEUSVR, https://www.thingiverse.com/thing:6099092) to compare to the results of Davis et al. (2019), an ammonite (open-source model by Thingiverse user BLPS, https://www.thingiverse.com/thing:6091760) to compare to

Hebdon et al. (2020), and an enrolled model of the trilobite *Placoparia cambriensis* (published by Esteve et al., 2018) to compare to Esteve et al. (2021). The 3D-printed models were scaled to match the sizes of the digital models in the relevant studies, but the models themselves were not identical. The trilobite model was also compared to the 25 mm sphere results because they are comparable in cross-section, and the published CFD results are on an outstretched rather than enrolled version of this model (Esteve et al., 2021), which thereby has strong differences in streamlining. For the published ammonite CFD data we used the drag values for the serplatycone model, as this was the most similar in overall morphology to our model in terms of being evolute with comparable coiling and chamber depths (Hebdon et al., 2020), though the models from Hebdon et al. (2020) did not have any surface texture, unlike our model.

The 10 and 25 mm spheres were rigged so they were ~150 mm from the bottom of the tank, the 50 mm sphere centre was 190 mm from the bottom, and the 75 mm sphere centre was 130 mm from the bottom. The horseshoe crab model was rigged with the model base 158 mm from the bottom of the tank, the ammonite base 118 mm, and the trilobite base 147 mm. These positions were a compromise between the height restrictions of the jig set-up (the lengths of carbon rods and low ceiling height) and ensuring the water depth was sufficient above and below the model to prevent edge effects from the tank or water surface. While we measured experimental drag and lift forces for the sphere models, we can present only the drag force results for the animal model experiments because the lift-measuring load cell installed in the jig had broken and could not be fixed before the end of the experimental runs. These vertical distances will be refined in future experimental work.

#### Data calibration and analysis

Several data calibration steps were required to gather accurate force data (see Supplementary Data):

- The load cells must be calibrated prior to use, but while already fixed in the jig. This is straightforward to carry out in Arduino (following the load cell menu instructions), though, due to the distortion of the drag load cell by the weight of the model, we had to 'negatively' calibrate this cell to ensure it could measure forces below zero.
- 2. A calibration series must be created for each load cell by measuring known masses. These series demonstrated a linear relationship between mass added and reading, though with a slope less than 1, likely due to the mounting of the load cells in the jig causing the load cells to be deformed less than when unfixed to the jig and thereby measuring a lower force than they should. To create the calibration series, we added known masses (10 g, 20 g, 30 g, 40 g, 50 g) to the affixed load cell in the compression direction and plotted the force readings made by the load cells. A regression line added to these plots is linear, and the slope was thereby taken as the calibration value for observed force measurements (see Supplementary Data).
- 3. We used the slope of the calibration series to calibrate all force readings for the load cells, and we set the zero point (intercept) for each load cell attached to each model by measuring the forces read when the model was placed in water of an equal depth (30 cm) with a velocity of 0 m/s. Finally, our

force readings were in gram force, so we converted these to N by dividing the gram force readings by 100. This gave a final calibration equation for the observed force readings of:

Final calibrated reading (N) = ((force reading (g force) - 0 m/s reading (g force)) × calibration series slope) / 100

Equation 2

4. We calculated the relative force at each velocity (calibrated reading at higher velocity/calibrated reading at lower velocity), as the magnitude of force change is a useful validation metric. We also calculated the drag and lift coefficients, to enable more effective comparison to published CFD simulation data, as follows:

$$C_d = \frac{2F_d}{\rho V^2 A}$$

Equation 3

$$C_L = \frac{L}{0.5\rho V^2 A}$$

Equation 4

where  $C_d$  = drag coefficient;  $F_d$  = drag force measurement (N);  $\rho$  = density of freshwater (998.06 kg/m<sup>3</sup> at 20.6 °C [measured by the UDVP] and 1 atm); V = water flow velocity (m/s); A = cross-sectional area of the model (m<sup>2</sup>);  $C_L$  = lift coefficient; L = lift force measurement (N).

5. When carrying out experiments on the spheres to validate the experimental protocol, we compared the results to drag forces calculated using drag coefficients taken from Goossens (2019). These are the drag forces we would expect to observe on a sphere if the experimental set-up was perfect (i.e., with no sources of error) (see Supplementary Data).

## **Results**

#### **Experimental validation of spheres**

The results of all experiments and calibrations are available in the Supplementary Data. The calibrated experimental drag and lift forces, relative forces, and drag forces calculated from coefficients in Goossens (2019) for all velocities and sphere diameters are presented in Table 1 and Figure 2. The less error inherent in the experimental protocol, the more similar to the Goossens (2019) calculated values we would expect the sphere drag results to be.

In general, we would expect the drag forces acting on the spheres to increase in line with flow velocity, and this is what we observe (Table 1; Fig. 2A). The theoretical relative drag suggests that, for all sphere diameters, the amount drag force increases is not linear, but lowers as velocity reaches 0.3 m/s. Only for a sphere of 10 mm diameter does theoretical relative drag increase from 0.1 m/s (3.3×) to 0.2 m/s (3.8×) (Table 1; Goossens, 2019). The experimental relative drag values are similar to the theoretical for the 50 mm sphere, though the actual calibrated median drag forces are lower than the theoretical forces by about 20×

(Table 1; Fig. 2A and B). The relative drag values for the 10 mm and 25 mm spheres are more different to the theoretical relative values; for the 10 mm sphere the 0.2 and 0.3 m/s values are reasonably similar, but the increase in drag from 0.05 to 0.1 m/s is twice that expected from Goossens (2019). For the 25 mm sphere, the drag is between doubling and tripling with each increase in velocity, while the values calculated from Goossens (2019) suggest this increase in drag should be higher across velocities of 0.05–0.2 m/s (Table 1; Supplementary Fig. 2). For the 75 mm sphere, the relative drag values do not follow the same pattern as for the other spheres; relative drag increases when going from 0.1 to 0.2 m/s velocity, then functionally does not decrease to 0.3 m/s velocity (Supplementary Fig. 2). The calibrated median drag forces for the 10 and 25 mm spheres are again lower than the theoretical drag forces (Fig. 2A and B); for the former between c. 8 and 15× lower and for the latter between c. 10 and 26× lower (Table 1). The experimental drag forces are  $3-11\times$ lower than the theoretical forces for the 75 mm sphere. Despite the differences in magnitude, the trends of the calibrated drag results do replicate those calculated from Goossens (2019) reasonably well (Fig. 2A and B). The theoretical C<sub>D</sub> should be about 0.44 for all velocities and sphere diameters, except for velocities =/< 0.1 m/s for the 10 mm sphere (Fig. 2C and D). Given the drag force results, the experimental C<sub>D</sub> values are of course lower than these theoretical C<sub>D</sub> values (Table 1; Fig. 2C and D). C<sub>D</sub> is highest for the 10 mm sphere, increasing to 0.1 m/s then falling, while for the other spheres the C<sub>D</sub> values are again reasonably consistently lower than the theoretical C<sub>D</sub> values by about 20× (Table 1; Fig. 2C and D).

Theoretical lift forces under standardised conditions are sparse, and predictions and experimental lift data vary widely (see Shi and Rzehak, 2019, 2020). However, it is apparent that the lift coefficient (C<sub>L</sub>) should decrease with increasing Re (which increases with velocity; see Goossens, 2019), and we see this pattern across all our experimental sphere results (Table 1, Fig. 3; except for one anomalous value at 0.2 m/s for the 50 mm sphere). The 75 mm diameter sphere moves into negative calibrated lift and C<sub>L</sub> values between a velocity of 0.1 and 0.2 m/s (Table 1; Fig. 3), though this seems reasonable in comparison to various predictions of C<sub>L</sub> that often trend into negative lift values (e.g., Lee and Balachandar, 2010; Shi and Rzehak, 2019, 2020). As for drag force and C<sub>D</sub>, our resulting lift forces and C<sub>L</sub> values are lower than we would expect from any comparable predictive data (Lee and Balachandar, 2010).

**Table 1:** Experimental drag and lift forces, and theoretical drag forces (from Goossens, 2019), for the 3D-printed spheres at flow velocities of 0.05–0.3 m/s. Cells shaded green show those within one order of magnitude of the relevant theoretical value; blue shading shows cells just over one order of magnitude smaller than the theoretical value; orange shading shows cells more than 20× lower than the theoretical value.

\*The theoretical relative drag is different for the 10 mm sphere because Newton's Law gives a drag coefficient (C<sub>D</sub>) of 0.44 for all Reynold's numbers (Re) over 1000, but for the 10 mm sphere at velocities up to 0.1 m/s the Re is below 1000, necessitating an increased C<sub>D</sub> and thereby a different relative drag.

Velocit	Theoretic	Calibrate	Theore	Relativ	Theoreti	Drag	Calibrat	Relativ	Lift
y (m/s)	al drag	d median	tical	e drag	cal drag	coefficie	ed	e lift	coefficient
	(N)	drag (N)	relativ			nt / CD			/ <b>C</b> L

	(Goossens,		e drog*		coefficie		median				
10 mm d	2019)  iameter sphe	*e	drag*		nt		lift (N)				
0.05	0.00686	0.000373			0.550	0.0192	0.00112		0.0577		
0.1	0.0220	0.00249	3.35	6.67	0.460	0.0320	0.00135	1.20	0.0173		
0.2	0.0878	0.00746	3.83	3.00	0.440	0.0240	0.00139	1.03	0.00447		
0.3	0.198	0.0126	2.25	1.68	0.440	0.0179	0.000943	0.677	0.00135		
25 mm diameter sphere											
0.05	0.0137	0.00129			0.440	0.0106	0.000987		0.00812		
0.1	0.0549	0.00307	4.00	2.39	0.440	0.00631	0.00148	1.50	0.00304		
0.2	0.220	0.00837	4.00	2.73	0.440	0.00430	0.00180	1.21	0.000923		
0.3	0.494	0.0215	2.25	2.56	0.440	0.00490	0.00229	1.28	0.000523		
50 mm d	50 mm diameter sphere										
0.05	0.0275	0.00116			0.440	0.00238	0.00148		0.00304		
0.1	0.110	0.00493	4.00	4.25	0.440	0.00239	0.000943	0.636	0.000484		
0.2	0.439	0.0241	4.00	4.89	0.440	0.00310	0.00503	5.33	0.000646		
0.3	0.988	0.0518	2.25	2.15	0.440	0.00296	0.00413	0.821	0.000236		
75 mm diameter sphere											
0.05	0.0412	0.0138			0.440	0.0126	0.00238		0.00217		
0.1	0.165	0.0244	4.00	1.77	0.440	0.00558	0.00112	0.472	0.000256		
0.2	0.659	0.0570	4.00	2.33	0.440	0.00325	-0.00260	2.32	-0.000149		
0.3	1.48	0.132	2.25	2.31	0.440	0.00334	-0.0157	6.02	-0.000398		

#### Comparison of experimental and computational data in palaeontology

In general, the magnitudes of the experimental drag force and C<sub>D</sub> values for the animal models are comparable to those obtained for the sphere models, excepting expected differences due to shape and streamlining (Tables 1 and 2). The congruency with experimental data compared to that published from CFD simulations varies depending on the animal model. For the ammonite model, the experimentally measured drag force and serplatycone CFD drag outputs are very similar in both trend and absolute values across all velocities (Table 2, Fig. 4A). The published absolute drag values of Hebdon et al. (2020) show high congruence with the experimentally derived force values of our study. However, the P. cambriensis and horseshoe crab model tests were comparable only using published C<sub>D</sub> values (Davis et al., 2019; Esteve et al., 2021), as the absolute drag values were not presented, nor were the relevant variables (e.g., water temperature, viscosity, model cross-sectional area) required to calculate them. The experimental C<sub>D</sub> values are at least two orders of magnitude lower than reported for the comparable CFD simulations (Table 2; Supplementary Fig. 3). The enrolled P. cambriensis model experimental C<sub>D</sub> is more similar to the results for the 25 mm sphere, particularly with the model facing the rear of the flume tank at velocities of 0.05 and 0.3 m/s where they are very similar (Fig. 4B), but the trilobite model results are higher for the intermediate velocities. When the model faced the anterior of the flume tank, the C<sub>D</sub> values were more comparable to those of the sphere at intermediate velocities, but notably lower than for the sphere at 0.05 m/s (Fig. 4B). Davis et al. (2019) only tested one velocity (0.13 m/s), but the simulated C<sub>D</sub> at this velocity is again much higher than the experimental results (Table 2, Supplementary Fig. 3).

**Table 2:** Experimental drag forces for the 3D-printed animal models at flow velocities of 0.05–0.3 m/s, and the simulated drag forces for comparable published CFD analyses on the same animals. Cells shaded green

show those within one order of magnitude of the relevant simulation value; orange shading shows cells more than 20× lower than the simulation value; cells with no comparable CFD simulation results are not shaded.

<sup>&</sup>lt;sup>3</sup> CFD comparison results from Esteve et al. (2021). *P. cambriensis* CFD results are on an outstretched model, rather than enrolled as tested here (both anterior- and posterior-facing in the flume tank), in both laminar and turbulent flows. Results were taken from their figure 1 using WebPlotDigitizer (Rohatgi, 2025). Left-column comparison results are those from the 25 mm sphere reported in this paper; see Table 1.

Velocity	Calibrated	Relative	CFD simulation drag results				
(m/s)	median drag	drag	Drag coefficient /				
	(N)		$\mathbf{C}_{\mathbf{D}}$				
Horseshoe	crab <i>Limulus po</i>	lyphemus <sup>1</sup>	CFD L.				
	_		polyphemus				
				C <sub>D</sub> (0° angle)			
0.05	0.00124		0.0122				
0.1	0.00228	1.83	0.00558				
0.13	0.00431	1.89	0.00624	0.276			
0.2	0.00842	1.95	0.00515				
0.3	0.0163	1.94	0.00444				
Ammonite <sup>2</sup>			CFD	CFD	Relative drag		
				serplatycone	serplatycone	for first	
				drag (N)	drag Ansys	column	
					(N)		
0.05	0.0000829		0.000507	0.000672	0.000284		
0.1	0.00323	39.0	0.00494	0.00246	0.000940	3.65	
0.2	0.0120	3.72	0.00460	0.00923	0.00342	3.76	
0.3	0.0242	2.01	0.00411	0.0206	0.0119	2.23	
	ilobite <i>Placopari</i>	a cambriensis³,	cephalon facing	25 mm sphere	CFD	CFD	
posterior of	f tank			experimental	outstretched 1	outstretched 1	
				C <sub>D</sub>	mm laminar	mm turbulent	
					CD	C <sub>D</sub>	
0.05	0.00120		0.00985	0.0103	0.518		
0.1	0.00448	3.72	0.00917	0.00615	0.478		
0.2	0.0119	2.66	0.00609	0.00420	0.439	0.474	
0.3	0.0233	1.96	0.00529	0.00478			
	ilobite <i>Placopari</i>	a cambriensis <sup>3</sup> ,					
anterior of							
0.05	0.000498		0.00408				
0.1	0.00249	5	0.00510				
0.2	0.00837	3.37	0.00429				
0.3	0.0189	2.26	0.00430				

# Velocity profiles for the sphere models

The presence of the sphere disturbed the flow for all sizes of sphere and for all inlet flow velocities. Disturbance can be seen as increased ranges of profile velocities as measured by the UDVP, in particular the presence of lower profile velocities in the area behind the sphere (Figs 5–7; Supplementary Figs 4 and 5). For higher inlet flow velocities, some profile velocities were negative, indicating the onset of turbulent flow

<sup>&</sup>lt;sup>1</sup> CFD comparison result from Davis et al. (2019). The value for experimental drag coefficient for the velocity of 0.13 m/s is interpolated.

<sup>&</sup>lt;sup>2</sup> CFD comparison results from Hebdon et al. (2020). Values are those given for the serplatycone model drag results (in dyne, converted to N) taken from their figure 7 (left column) and Ansys values reported in their Appendix I (right column).

(Figs 5–7; Supplementary Figs 4 and 5). At low inlet velocities (0.05, 0.1, and 0.2 m/s) disturbance was minimal for the 10 mm and 25 mm spheres, with the lowest profile velocities only very slightly lower than at depths not behind the sphere. At the inlet velocity of 0.3 m/s, negative profile velocities are seen across the vertical profile at all distances behind the sphere.

At inlet velocities of 0.05 m/s and 0.1 m/s for the 50 mm sphere the mean profile velocities were slower than the inlet velocities with the UDVP close behind the sphere, and at 3 diameters (150 mm) and 5 diameters (250 mm) behind the sphere, but not at >20 diameters (>1000 mm) (Fig. 6A and B; Supplementary Fig. 5). At the higher inlet velocities (0.2 m/s and 0.3 m/s) the profile velocities 3 diameters behind the sphere showed a broad range of velocities, including some around 0 m/s and sparse negative velocities. This disruption was reduced at 5 diameters behind the sphere, and at >20 diameters behind the sphere very little disruption to the flow was observed.

The 75 mm sphere disrupted the flow 2 diameters (150 mm) behind it at all inlet velocities, with numerous negative values and a lower mean profile velocity than inlet velocity (Fig. 6C and D; Supplementary Fig. 5). The disruption at 250 mm behind the sphere was less for the two slower inlet velocities (0.05 m/s and 0.1 m/s), with only positive profile velocities recorded, and at over 1000 mm behind the sphere no disturbance to the flow was identified. However, for inlet velocities 0.2 m/s and 0.3 m/s negative profile velocities were recorded at 250 mm and more than 1000 mm behind the sphere, although the mean profile velocities were very similar to the inlet velocities.

#### Velocity profiles for the animal models

All fossil models introduced disturbance to the flow; this is most apparent for higher velocities (0.2 and 0.3 m/s) and at closer distances to the model (Fig. 7). The ammonite and horseshoe crab disturbed the flow less than the enrolled trilobite (in either orientation), with all shapes disturbing the flow less than spheres of a comparable diameter (Fig. 7A, B, E, F; Supplementary Figs 6 and 8). At inlet velocities of 0.05 m/s, 0.1 m/s and 0.2 m/s the mean profile velocities behind the enrolled trilobite (cephalon facing anterior) were slower than the inlet velocity at distances 170 mm, 200 mm, 225 mm, and 250 mm behind the trilobite. At >1000 mm behind the trilobite most of the velocity profile had returned close to the inlet velocity, except for depths furthest from the tip of the probe for the 0.05 m/s and 0.2 m/s data (Fig. 7C and D; Supplementary Fig. 7). No negative profile velocities were recorded at any of these three inlet velocities. At an inlet velocity of 0.3 m/s negative profile velocities were recorded at distances 170, 200, and 225 mm behind the trilobite, with most negative profile velocities at 170 mm behind the trilobite. The flow at >1000 mm appears undisturbed (steady velocity profile, with mean profile velocity equal to the inlet velocity), with only slight disturbance at 250 mm behind the trilobite (broader range of profile velocities including some slower ones, but mean profile velocity very close to the inlet velocity). UDVP data for the enrolled trilobite with the cephalon facing posterior were similar. At inlet velocities of 0.05, 0.1 and 0.2 m/s the mean profile velocity was slower than the inlet velocity at distances 170, 200, 225 and 250 mm behind the trilobite, with no negative

velocities. At 0.3 m/s, negative profile velocities were recorded at all distances sampled behind the trilobite except for >1000 mm (Supplementary Fig. 7). More negative velocities were recorded for the enrolled trilobite with the cephalon facing posterior than anterior.

At all inlet velocities, no negative profile velocities were recorded behind the horseshoe crab or the ammonite (Fig. 7A, B, E, F). Profile velocities slower than the inlet velocity were recorded at distances up to 250 mm behind the model of the horseshoe crab at all inlet velocities. However, the noise due to measuring profile velocities far from the tip of the probe was comparable to the reduction in profile velocity due to disturbance by the model (Fig. 7E and F; Supplementary Fig. 8). Finer scale interpretations than these—for example, which part of the flow is disturbed by a specific part of the model—are not possible with the current experimental set-up. The bottom distance as measured by the probe often contains noise (sometimes up to 0.03 m) and so alignment with the exact position of the model is affected by this error. Profile velocities very close to and furthest from the tip of the probe are also more variable than those  $\sim 0.01-0.02 \text{ m}$  from the tip of the probe.

# **Discussion**

### Efficacy of the experiments

Overall, the sphere results were similar in their drag force patterns to the theoretical values, particularly for spheres with a diameter larger than 10 mm (Table 1; Fig. 2), though much less so in their absolute magnitudes, the experimental drag results being usually at least one to two orders of magnitude lower. The lift force coefficient results seem to fit a consistent and reasonable trend (Table 1; Fig. 3) given the ranges of  $C_L$  we expect from theoretical and engineering studies (e.g., Kurose & Kumori, 1999; Shi & Rzehak, 2019), though these are harder to compare to theoretical results. Not even the theoretical drag forces acting on spheres of these sizes are fixed; the expected  $C_D$  values still differ between published studies (e.g., see Goossens, 2019). Overall, this indicates that the experimental set-up, with some improvements needed to get the magnitude of the force readings closer to the theoretical values or determine a consistent modifier for the experimental values, is doing a reasonable job at measuring the real-world forces that would act on the model.

While some animal models (such as enrolled trilobites) will be comparable to results for spheres, and thus sphere data could be used for validation, not all will be given the presumed evolutionary pressures of a marine-realm causing morphological adaptation to hydrodynamic pressures. However, the experiments using sphere models thereby give us confidence in the preliminary experimental set-up, providing a baseline for evaluating the reliability of the force results for animal models. We therefore progressed to animal models to evaluate the closeness between EFD results and comparable published CFD simulations. The pelagic ammonite model experiments were notably similar to the comparable CFD simulations (from Hebdon et al., 2020), with the calibrated drag force trends and absolute values being very close (Table 2; Fig. 4A). However, the other animal model results were less comparable to the CFD simulations (Table 2; Fig. 4B;

Supplementary Fig. 3). This may simply be due to the experimental set-up, as we positioned the horseshoe crab and trilobite models midway between the base of the tank and the surface of flowing water to enable comparison to the sphere models. In comparison, the CFD simulations (Davis et al., 2019 and Esteve et al., 2021, respectively) positioned these models in a benthic life habit close to the virtual tank base, where interaction between the fluid and the base of the tank would have impacted the drag forces experienced by the animals. Additionally, the *P. cambriensis* results are presumably much different from the CFD simulations because our model was enrolled (due to limited model availability), while the Esteve et al. (2021) model was outstretched. Additionally, the trilobite model tests compare the C<sub>D</sub> results and C<sub>D</sub> is directly influenced by cross-sectional area, which is notably different for the two types of models. The experimental C<sub>D</sub> values for *P. cambriensis* are generally more similar to those of the similar-sized sphere experiments for this reason (Fig. 4B).

Developing the experimental methods presented here is crucial to palaeoecological hypothesis-testing, as they will enable an independent line of evidence for validation of CFD simulations and exploration of extinct animal hydrodynamic adaptations. CFD simulations using models of long-extinct animals project forces acting on these animals, but at slow flow regimes the forces are difficult to reconstruct due to the low Reynolds numbers. EFD results from experiments such as these using identical 3D-models in real-world flow scenarios allow comparison to simulated forces and validation of their reliability. However, the majority of palaeoecological CFD studies do not carry out any experimental validation to support their simulations. Amongst those studies discussed here, only Davis et al. (2019) carried out validation, comparing PIV data to simulated velocity profiles. Unfortunately, most palaeoecological CFD work is not reported in a way that is easily comparable to experimental work (e.g., for many studies approximate force coefficients must be taken from the provided plots rather than all data being given, such as for Davis et al., 2019, and Esteve et al., 2021), and some studies do not provide their animal models and so cannot be validated secondarily and these models cannot be used by other researchers.

#### **Velocity profiles and future improvements**

The velocity profiles presented here can be used as a complementary way to validate CFD simulations. Some ecological studies (e.g., Rahman et al., 2015; Dynowski et al., 2016; Davis et al., 2019; Gibson et al., 2023) have used velocity profile data from other experiments or conducted their own in order to validate simulations, and such an approach is certainly valid when interpreting the impact of shape on feeding currents, and looking at flow patterns and generation of vortices or the onset of turbulence. Indeed, if the CFD simulations can generate accurate flow patterns and identify the point at which the flow recombines after separation, or the extent of turbulence at different parts of the wake, then more confidence can be gained from the drag and lift forces that such simulations present. It is our ultimate aim that the UDVP data and drag and lift forces can be used in tandem to validate simulations, but as we continue to improve our drag and lift force data collection and experimental design, these velocity profiles provide valuable data for validating CFD simulations on a range of invertebrate taxa of different shapes at a range of Reynolds numbers.

The velocity-measuring setup used in these experiments does result in some errors and uncertainties that limit the resolution of the results, whilst there are also physical limitations to what data are possible to collect. These result from limitations of the Nortek Vectrino probe itself, as well as the interaction between the probe, tank, and jig. The range of velocities recorded by the probe seems to be broader at distances closest to the probe and furthest away. Of the 31 mm total range, the probe appears to perform best at distances between 10–20 mm from the focal point. The probe also has a higher error relative to the inlet velocity at lower velocities (the 0.05 m/s inlet velocity data often has a broad range of values even >1000 mm away from models). As demonstrated for the ammonite model (Fig. 7A and B), it is possible to record velocity data at multiple heights to increase the overall range sampled by the velocimeter, and then to stack these data. Thus, in future we will use a smaller sampling range for the velocimeter (up to 21 mm) to improve the precision while also collecting at multiple depths. A stand with a crank handle enabling precise movement of the probe vertically, without needing to unclamp and manually move the UDVP to change measurement depth, will facilitate collection of a broader range of depths at higher precision.

To enable this stacking of velocity measurements and accurate understanding of the resolution of flow disturbance around the model, the bottom distance measured by the probe is important. However, the probe occasionally measured inaccurate bottom distances, (e.g., for the 25 mm sphere; Fig. 5C and D) giving an erroneous depth for the flow. This could result from the metal base of the flume tank, which may have provided too reflective a surface in some instances. To resolve this, a black bottom will be added to the tank in future.

A final limitation of the UDVP experimental set-up relates to the size of the probe and equipment needed to secure both the jig and the probe. These place a physical limit on how close to the model it is possible to gather velocity data; anything closer to the model than 150 mm was not possible. This means that the velocimeter was useful in gathering data on the distance behind the model where flow became undisturbed (the separation caused by the model ended), the disappearance of negative velocities (interpreted as vortices shedding from the model), the overall profile behind the model, and for checking the inlet velocity was correct. However, the velocimeter was not able to determine the flow disturbance immediately behind the model, and thus it is here that CFD approaches, which present a visualisation of the whole flow field, provide complementary information to the experimental data, with experimental data providing validation (distance before separation finishes, presence of vortices at different flow speeds, dissipation of vortices behind the model).

# Future experimental protocol refinement

The preliminary experimental protocol presented here has demonstrable utility in comparing to CFD simulation results for ecological and evolutionary studies. However, the validation sphere results in particular make clear that the protocol can be improved in several ways, along with those improvements

discussed above for the velocity profile measurements. While carrying out experiments, it was clear that the mechanism of fixing the model and rod to the jig containing the load cells impacted the forces measured. We were obliged to record all force data for each model without detaching it from the jig, instead changing the flow velocity in between readings, because the tightness of the screw attaching the rod to the jig impacted the force measurements (though not to changing orders of magnitude). This was deemed sufficient for the current experiments because the force measurements were internally consistent if the rod was not removed, but in future experiments we will directly attach the load cells to the rod such that each model has its own measurement devices permanently affixed, and this component then attached to the jig.

In terms of the data readings, we presented the results for median calibrated drag, though we also give the minimum and maximum values for the recorded ranges in the Supplementary Data. The median values were used here to compare to the theoretical values because the recorded extremes of the ranges were impacted by the small movements of the jig and carbon rod, particularly at the higher velocities, whereas the range limits were affected by these. However, the SparkFun circuitry equipment support automatic logging of readings to a microSD card inserted in the OpenLog Artemis, and so in future we will be able to take a final value more representative of the range of readings and less sensitive to extremes, such as by using the modal value. Carrying out the repeats of all experiments, both of the validation spheres and the animal models, would also improve the reliability of the results. Additionally, we will reduce the reading error resulting from movement and bending of the carbon rod by shortening it as much as possible from its current 50 cm length. For models suspended within the flow in the tank rather than at the tank-bottom, this can easily be accomplished by placing the jig directly on top of the flume tank, allowing reduction of the rod length by an estimated 20–30 cm.

As the velocity profile data were collected using commercial and bespoke (Nortek) equipment and software, the challenges and opportunities are quite different to recording of the drag and lift forces. To a certain extent, use of commercial equipment gives results 'out of the box', allowing generation of results more quickly. However, using proprietary software also led to limitations. For example, the software only runs on contemporary Windows operating systems, only allowed collection of data over a 30 mm vertical profile, and only in .ntk format. Additional time-consuming steps were required to manually convert each file to ASCII format, and then bespoke R code was needed to convert these ASCII files into something that could be interpreted and plotted.

Overall, the error inherent in the experimental system, is, at present, not precisely quantifiable, so for the current time we suggest that a series of experiments using sphere models are carried out for each new laboratory set up for palaeoecological hypothesis-testing to enable exploration of the error in comparison to theoretical results, as shown here. This means that, while the error cannot be removed entirely, the experimenter has baselines for interpreting their subsequent organism-model results. However, our ultimate aim in making these discussed future improvements is to standardise the error across the experimental

protocol. We will never be able to measure the exact theoretical force values because they will always be depressed by having to connect the model to the measuring equipment rather than it being free to move; this is the only possibility with contemporary force-measuring equipment. But if we can derive a consistent modifier with which to increase the force values to account for the magnitude of force lost by the experimental set-up, then we can use this experimental protocol to produce robust force validation data for animal model fluid dynamics studies.

## Conclusion

This is the first study presenting an Experimental Fluid Dynamics protocol for palaeoecological hypothesistesting, and validation of palaeoecological CFD simulations using both drag and lift forces and velocity
profiles behind the models. For the most part, our experimental results tracked the theoretical drag force
results reasonably well, though were too low in magnitude. The ammonite experimental drag was almost
exactly that reported from CFD simulations (from Hebdon et al., 2020), likely because the experimental
conditions were very similar (comparable models, in pelagic settings), while the tests comparing the other
animal models had less similar results due to the different experimental conditions (pelagic versus benthic
positioning, enrolled trilobite model). However, this work is still in progress, with needed refinement of the
mounting of the load cells and the model and rod to the jig, taking a median of all logged force readings, and
carrying out repeats of all future experiments to assess variance. We hope to inspire other palaeoecological
studies using fluid dynamics methods to consider carrying out experimental validation work, and provide full
details of our experimental set-up to support this.

# Acknowledgements

The authors wish to gratefully acknowledge assistance from those at the University of Portsmouth. John Fearnley from the manufacturing lab is thanked for producing the jig CAD in consultation with the authors, building the physical jig, carrying out the 3D printing, and providing frequent technological support. Chris Warden and Andreas Lee, School of Mathematics and Physics, are thanked for providing much needed help with circuitry. Gary Etienne is thanked for technical assistance with the flume tank lab. Roy Smith, School of the Environment and Life Sciences, is thanked for support and for planning of future 3D printing. Steve Mitchell, School of Civil Engineering and Surveying, provided access to and assistance with the use of the Nortek Vectrino Profiler Fixed Probe.

# **Funding**

HBD was funded under a Swiss National Science Foundation Sinergia grant (198691). SP was funded by a Herchel Smith Postdoctoral Fellowship (University of Cambridge) and National Environment Research Council Independent Research Fellowship NE/X017745/1 (University of Exeter) and NE/X017745/2 (University College London). Equipment and travel costs were supported by a 2023 research grant from the Geological Society awarded to HBD, the Herchel Smith Postdoctoral Fellowship, and a School of the Environment and Life Sciences Research and Innovation Accelerator fund awarded to NJM.

# **Author contributions**

Conceptualisation – HBD, SP; Methodology – HBD, SP, NJM; Formal analysis – HBD, SP, NJM; Investigation – HBD, SP, NJM; Resources – HBD, SP, NJM; Writing – Original draft – HBD; Writing – review & editing – HBD, SP, NJM; Visualisation – HBD, SP; Project administration – HBD, SP, NJM; Funding acquisition – HBD, SP, NJM.

# **Figures**

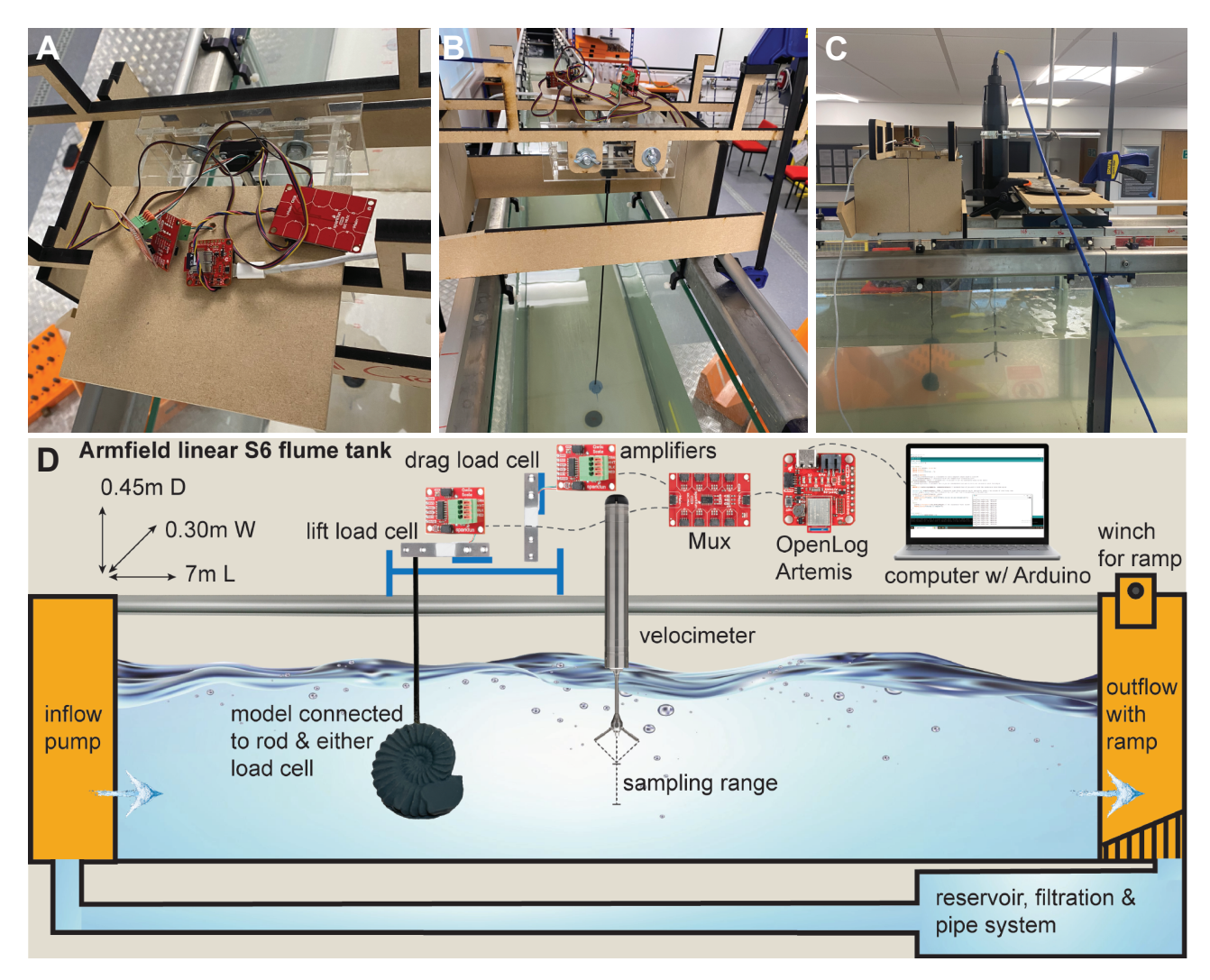


**Figure 1:** Experimental set-up. A, SparkFun circuitry used to log forces connected to load cell attached to jig above flume tank, with load cell attached to rod with model; white cable connects circuitry to computer. B, circuitry on jig suspended above flume tank, with model attached to rod suspended in the water flow. C, side-view of model suspended in water flow, with velocimeter mounted behind the model in the flow; distance of velocimeter to model can be changed by moving the platform the velocimeter rests on. D, diagrammatic representation of experimental set-up; the load cells are in reality held in the jig positioned above the flume tank, but the diagram accurately represents their orientations in contrast to the model and direction of water flow; dashed lines below the velocimeter show an example velocity sampling range.

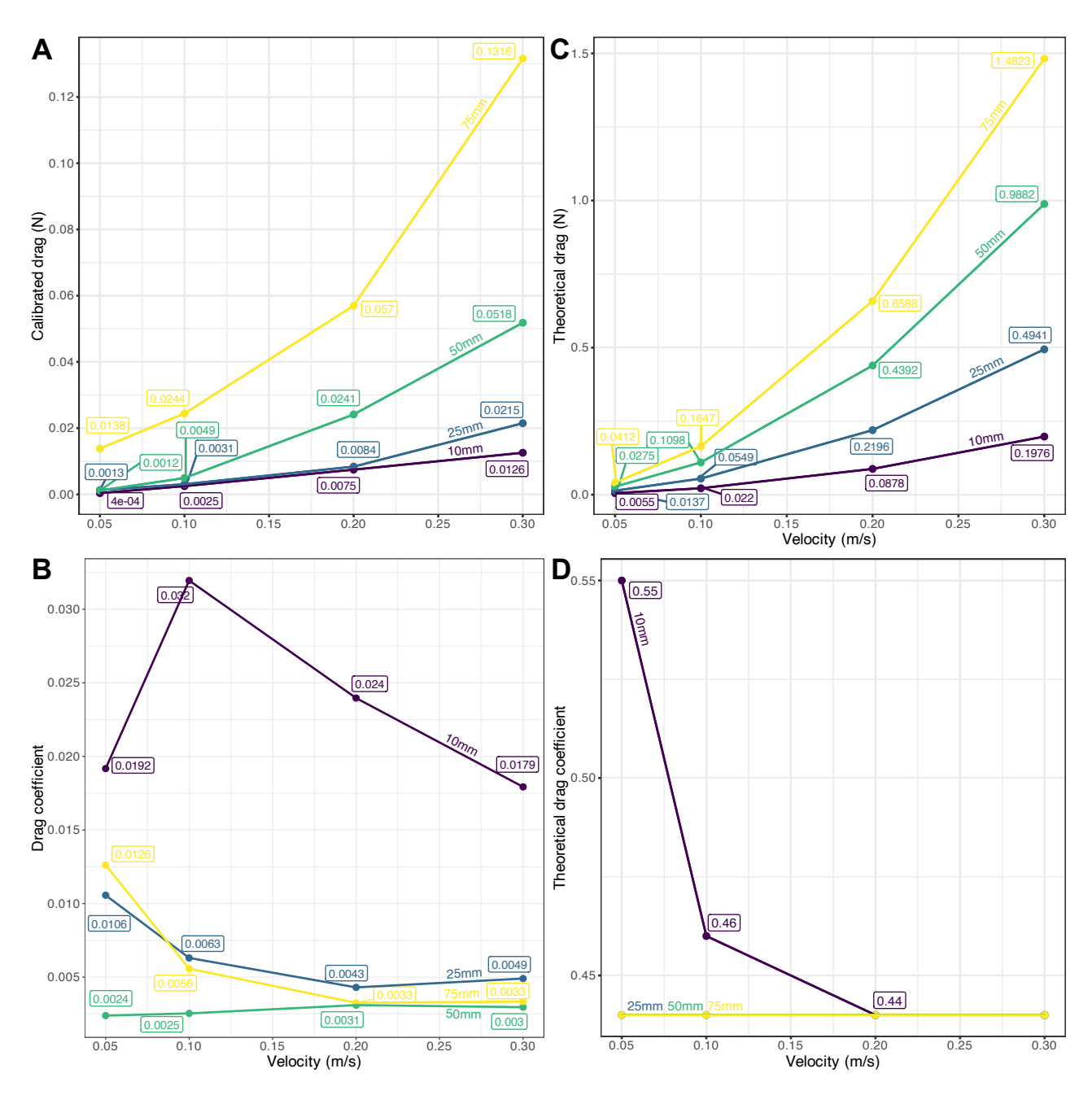


**Figure 2:** Comparison between EFD results and theoretical calculations for the sphere models. A and B, Experimental values for calibrated drag and drag coefficient, respectively; C and D, theoretical drag and drag coefficient, respectively, calculated from Goossens (2019). All lines are labelled with the diameters of their corresponding spheres, and all plotted points are labelled with their values. Scale bars are not comparable across A and B, or C and D; given the order of magnitude differences between the values, the experimental trends would not be visible.

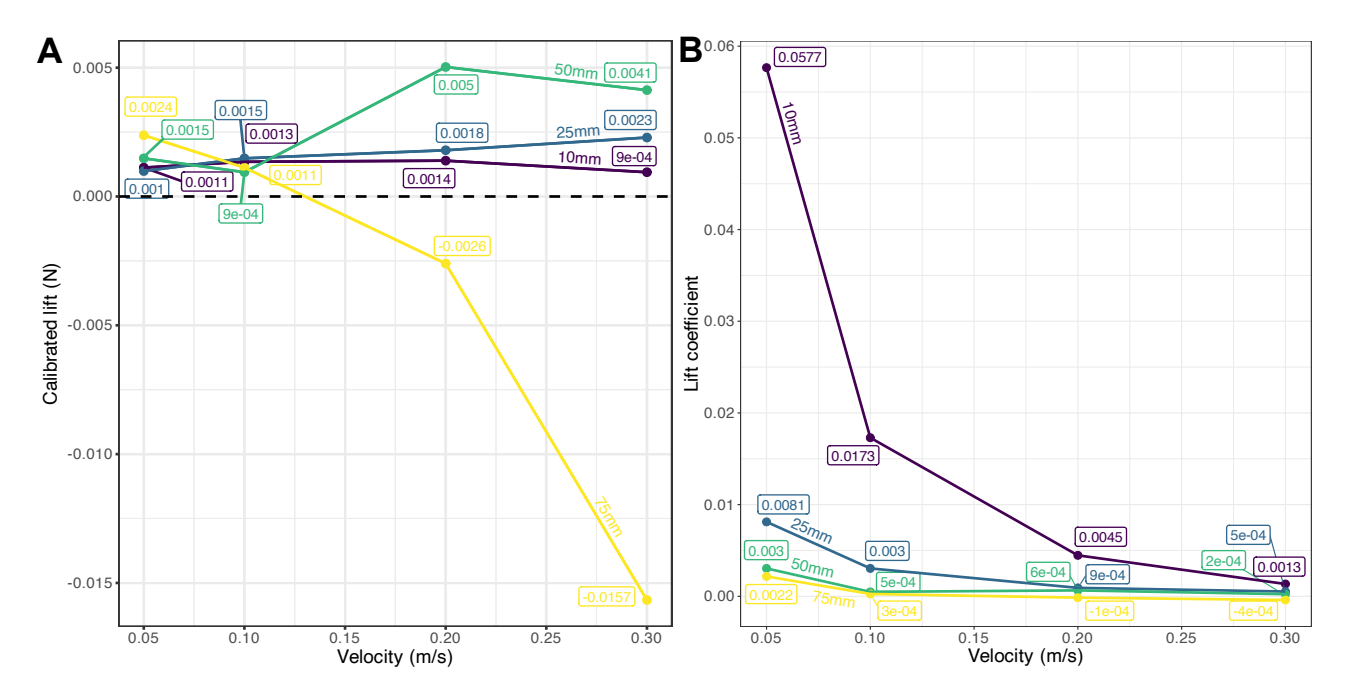


**Figure 3:** Experimental values for calibrated lift (A) and lift coefficient (B). All lines are labelled with the diameters of their corresponding spheres, and all plotted points are labelled with their values. Dashed line on A represents 0 N lift.

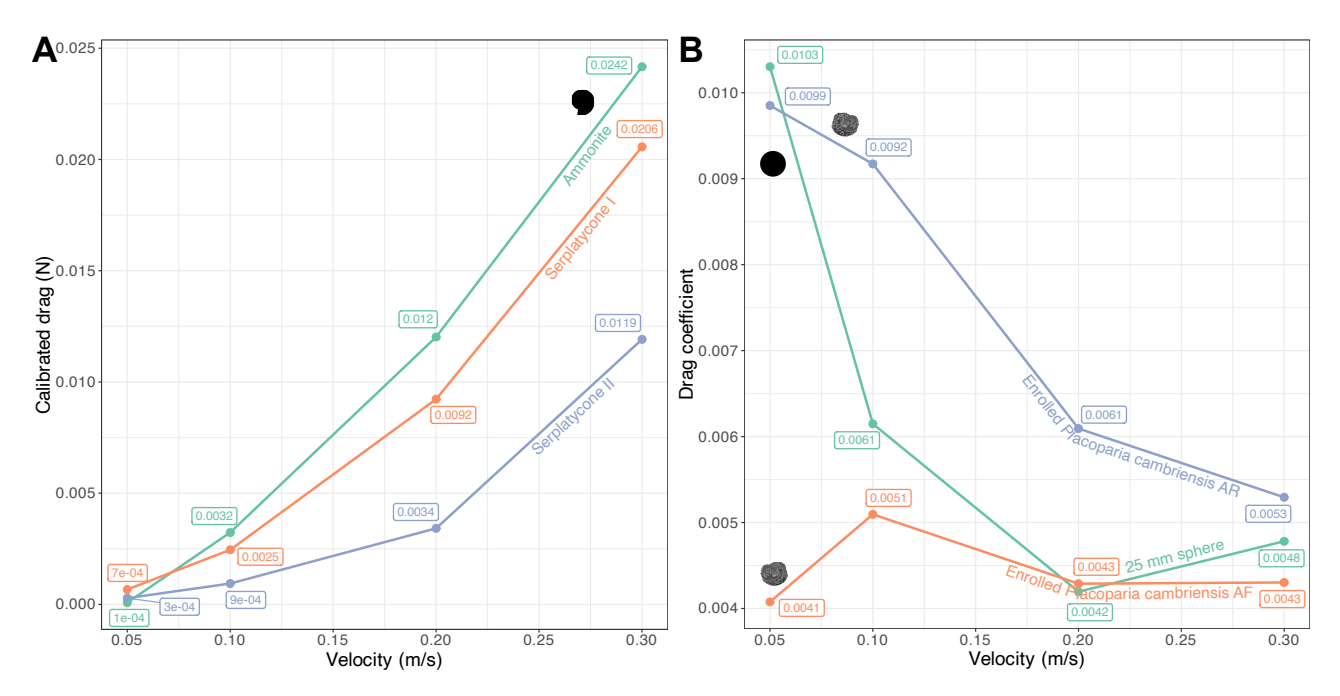


**Figure 4:** Comparison of drag values from EFD and published CFD simulations. A, experimental and CFD calibrated drag for the ammonite model and for a serplatycone model under two regimes (from Hebdon et al, 2019). B, experimental drag coefficient for the 25 mm sphere and enrolled *Placoparia cambriensis* with its cephalon facing both the front (AF) and rear (AR) of the flume tank, the simulated drag coefficient for the outstretched *P. cambriensis* (from Esteve et al., 2021) is plotted in Supplementary Figure 3A as its much higher C<sub>D</sub> values (0.44–0.52) prevent interpretation of the other model tests. The comparison of drag coefficient to that reported by Davis et al. (2020) is also plotted in Supplementary Figure 3B.

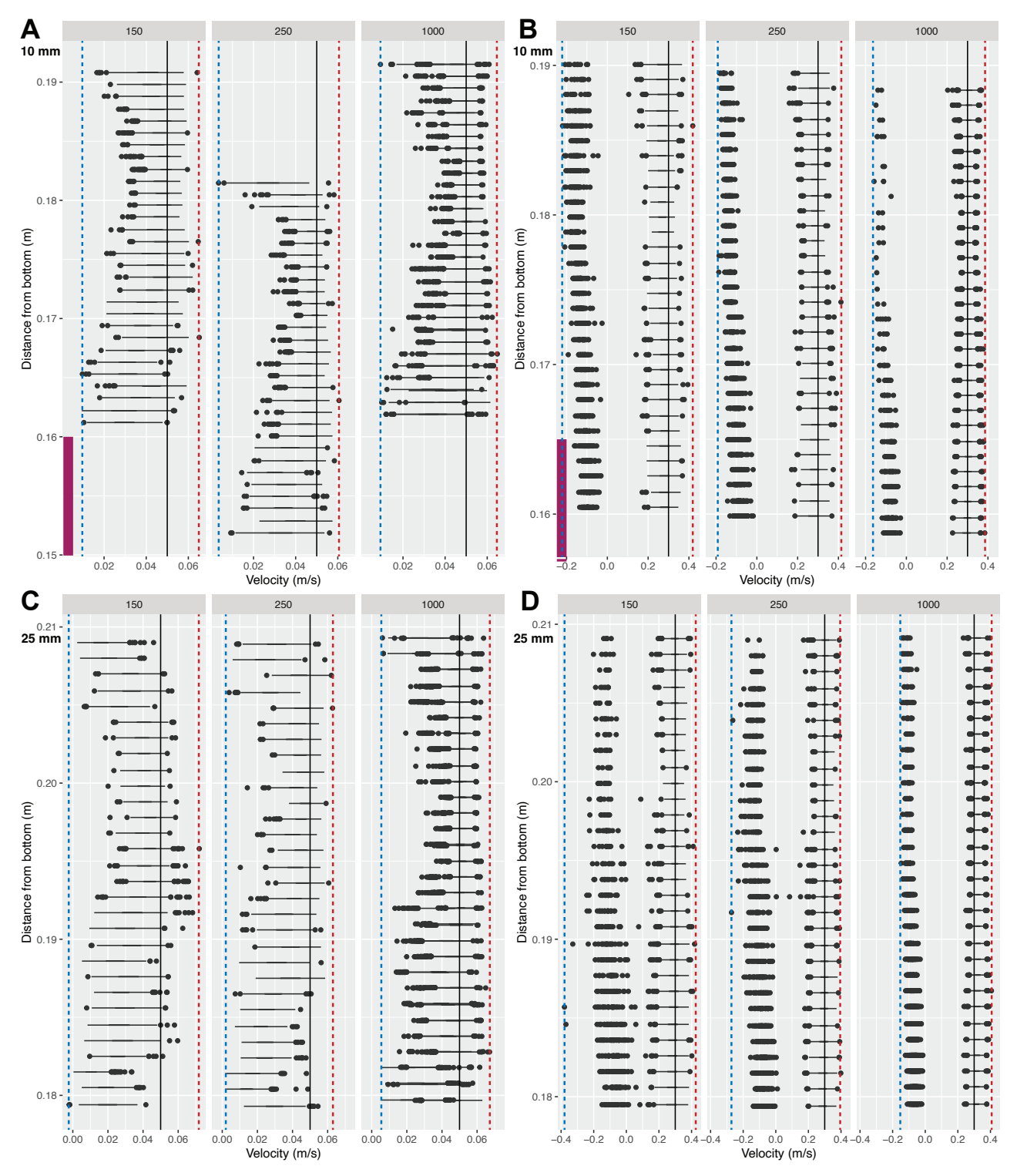


**Figure 5:** Velocity profiles for the 10 and 25 mm spheres: A, 10 mm sphere at 0.05 m/s; B, 10 mm sphere at 0.3 m/s; C, 25 mm sphere at 0.05 m/s; D, 25 mm sphere at 0.3 m/s. The velocity profiles for both spheres at 0.1 and 0.2 m/s are plotted in Supplementary Figure 4. Horizontal bars effectively denote the range of velocities (within 1.5× the interquartile range extending outside the first and third quartiles), while dots are values lying outside of this range. Black solid vertical lines indicate the inflow pump velocity; red dotted lines show the maximum velocity achieved, and blue dotted lines show the minimum velocity achieved. Purple bars show the distances from the bottom and vertical heights of the sphere models, however, this is not plotted for the 25 mm sphere (same distance from bottom as the 10 mm sphere) because the distance

from bottom measured by the UDVP (y-axis in C and D) is incorrect (likely due to reflectance of the silver tank-bottom).

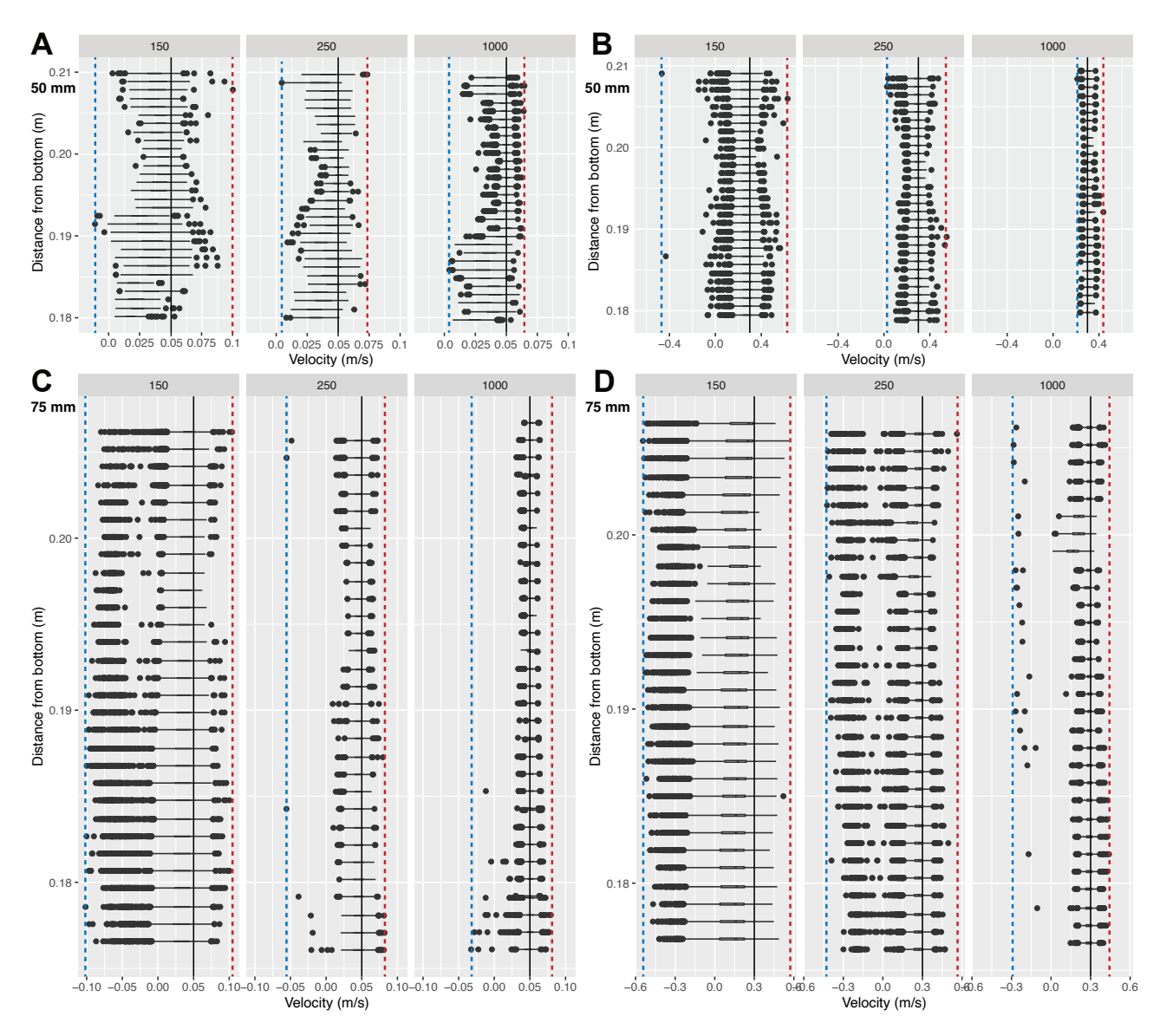


**Figure 6:** Velocity profiles for the 50 and 75 mm spheres: A, 50 mm sphere at 0.05 m/s; B, 50 mm sphere at 0.3 m/s; C, 75 mm sphere at 0.05 m/s; D, 75 mm sphere at 0.3 m/s. The velocity profiles for both spheres at 0.1 and 0.2 m/s are plotted in Supplementary Figure 5. Horizontal bars effectively denote the range of velocities (within 1.5× the interquartile range extending outside the first and third quartiles), while dots are values lying outside of this range. The sphere models for each test extend across the entire (within a few mm) range of the measured velocity profile, so are not displayed. Black solid vertical lines indicate the inflow pump velocity; red dotted lines show the maximum velocity achieved, and blue dotted lines show the minimum velocity achieved.

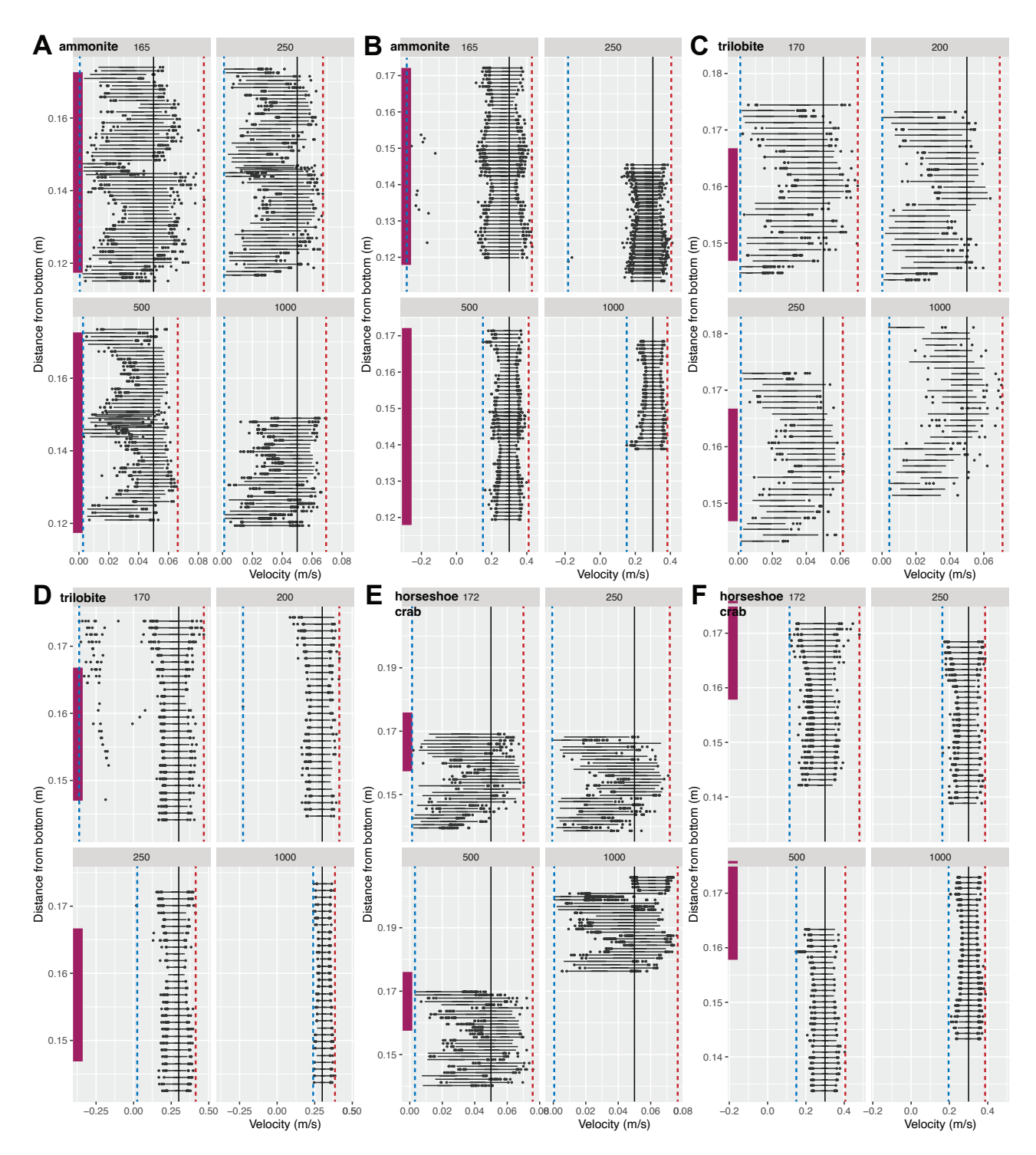


**Figure 7:** Velocity profiles for the animal models: A, ammonite model at 0.05 m/s; B, ammonite model at 0.3 m/s; C, enrolled *Placoparia cambriensis* trilobite model (with cephalon orientated towards the tank anterior) at 0.05 m/s; D, same enrolled trilobite at 0.3 m/s; E, horseshoe crab model at 0.05 m/s; F, horseshoe crab model at 0.3 m/s. The profiles taken at 375 mm, 225 mm, and 375 mm behind the models respectively were removed for space, but all velocity profiles for the animal models, including those at 0.1 and 0.2 m/s, are plotted in Supplementary Figures 6–8. Horizontal bars effectively denote the range of velocities (within 1.5× the interquartile range extending outside the first and third quartiles), while dots are values lying outside of this range. Black solid vertical lines indicate the inflow pump velocity; red dotted lines show the

maximum velocity achieved, and blue dotted lines show the minimum velocity achieved. Purple bars show the distances from the bottom and vertical heights of the animal models.

# **Supplementary material**

All supplementary material for this study are freely accessible on the Open Science Framework (OSF) at <a href="https://doi.org/10.17605/OSF.IO/CYW7N">https://doi.org/10.17605/OSF.IO/CYW7N</a>. All Supplementary Figures are found within the folder Drageetal. EFD2025 Supplementary Figures.zip, with their captions below.

Supplementary Figure 1: Images of digital 3D models used for experiments presented herein. A, ammonite model (open-source model by Thingiverse user BLPS, https://www.thingiverse.com/thing:6091760); B, enrolled *Placoparia* model (published by Esteve et al., 2018); C, horseshoe crab *Limulus polyphemus* model (open-source 3D-scan by Thingiverse user GEUSVR, https://www.thingiverse.com/thing:6099092); D, spheres with diameters of 10 mm, 25 mm, 50 mm and 75 mm; E, example 3D-printed physical model of A, attached to the carbon rod and used in experiments, with a scale bar of 1 cm.

Supplementary Figure 2: Relative increase in drag force acting on each of the four spheres for each inlet velocity. The relative increase at 0.05 m/s would be infinite as this represents the slowest inlet velocity tested. A, experimental, calibrated drag forces acting on each sphere; B, theoretical drag forces derived from Goossens (2019). Dashed lines on A show the relative drag force increases expected based on B.

Supplementary Figure 3: Comparison of experimental results to CFD simulations. A, experimentally derived drag coefficient for the enrolled *Placoparia* trilobite model (with anterior facing both the anterior and rear of the flume tank) and the 25 mm sphere, and the simulated drag coefficient for the outstretched *Placoparia* model published in Esteve et al. (2021); B, experimentally derived drag coefficient for the *Limulus polyphemus* model, and the simulated drag coefficient for the same published in Davis et al. (2019).

Supplementary Figure 4: Additional velocity profiles for the 10 and 25 mm spheres: A, 10 mm sphere at 0.1 m/s; B, 10 mm sphere at 0.2 m/s; C, 25 mm sphere at 0.1 m/s; D, 25 mm sphere at 0.2 m/s. Horizontal bars effectively denote the range of velocities (within 1.5× the interquartile range extending outside the first and third quartiles), while dots are values lying outside of this range.

Supplementary Figure 5: Additional velocity profiles for the 50 and 75 mm spheres: A, 50 mm sphere at 0.1 m/s; B, 50 mm sphere at 0.2 m/s; C, 75 mm sphere at 0.1 m/s; D, 75 mm sphere at 0.2 m/s. Horizontal bars effectively denote the range of velocities (within 1.5× the interquartile range extending outside the first and third quartiles), while dots are values lying outside of this range.

Supplementary Figure 6: All measured velocity profiles for the ammonite model. A, at 0.05 m/s; B, at 0.1 m/s; C, at 0.2 m/s; D, at 0.3 m/s. Horizontal bars effectively denote the range of velocities (within 1.5× the interquartile range extending outside the first and third quartiles), while dots are values lying outside of this range.

Supplementary Figure 7: All measured velocity profiles for the *Placoparia* trilobite model (with cephalon orientated towards the tank anterior). A, at 0.05 m/s; B, at 0.1 m/s; C, at 0.2 m/s; D, at 0.3 m/s. Horizontal bars effectively denote the range of velocities (within 1.5× the interquartile range extending outside the first and third quartiles), while dots are values lying outside of this range.

Supplementary Figure 8: All measured velocity profiles for the horseshoe crab (*Limulus polyphemus*) model. A, at 0.05 m/s; B, at 0.1 m/s; C, at 0.2 m/s; D, at 0.3 m/s. Horizontal bars effectively denote the range of velocities (within 1.5× the interquartile range extending outside the first and third quartiles), while dots are values lying outside of this range.

Supplementary Data (Drageetal.\_EFD2025\_SupplementaryData.xlsx): Workbook containing the following two files as two sheets (SupplementaryData1.csv and [...]2.csv). Provided in addition to the separate .csv files to retain formatting to guide the reader. Also contains a third sheet with the theoretical drag coefficient values taken from Goossens (2019) for spheres, with calculations of the resulting theoretical drag forces.

Supplementary Data I (Drageetal.\_EFD2025\_SupplementaryData1.csv): Sheet containing the distances of models from the base of the flume tank, and the force results (plus calibrations) for all sphere models tested in the study.

Supplementary Data II (Drageetal.\_EFD2025\_SupplementaryData2.csv): Sheet containing the distances of models from the base of the flume tank, and the force results (plus calibrations) for all animal models tested in the study.

Supplementary Data III (Drageetal.\_EFD2025\_SupplementaryData3.zip): All ASCII files outputted by the Vectrino Profile, containing velocity profile data, for each model test. These folders also contain the exported .csv files used to interpret and plot the velocity profiles.

Supplementary Code folder (Drageetal.\_EFD2025\_SupplementaryCode.zip): R code developed to extract velocity, profile depth, and bottom depth data from the proprietary ASCII outputs of the Vectrino Profiler and export these data as .csv files. One file is provided to parse the ASCII files and export data as .csv (Parse\_ASCII\_in\_R.R) and additional files contain code used to plot the resulting .csv formatted data (Plot\_ASCII[...].R).

# References

Balsam, W.L. & Vogel, S. 1973. Water movement in archaeocyathids: evidence and implications of passive flow in models. *Journal of Paleontology* 47:5, 979–984.

Bicknell, R. D., Holmes, J. D., Edgecombe, G. D., Losso, S. R., Ortega-Hernández, J., Wroe, S., & Paterson, J. R. (2021). Biomechanical analyses of Cambrian euarthropod limbs reveal their effectiveness in mastication and durophagy. *Proceedings of the Royal Society B* 288:1943, 20202075. https://doi.org/10.1098/rspb.2020.2075.

Bicknell, R.D.C., Schmidt, M., Rahman, I.A., Edgecombe, G.D., Gutarra, S., Daley, A.C., Melzer, R.R., Wroe, S. & Paterson, J.R. 2023. Raptorial appendages of the Cambrian apex predator *Anomalocaris* canadensis are built for soft prey and speed. *Proceedings of the Royal Society B* 290:2002. https://doi.org/10.1098/rspb.2023.0638.

Davis, A.L., Hoover, A.P. & Miller, L.A. 2019. Lift and drag acting on the shell of the american horseshoe crab (*Limulus polyphemus*). *Bulletin of Mathematical Biology* 81, 3803–3822. https://doi.org/10.1007/s11538-019-00657-2.

Dynowski, J.W., Nebelsick, J.H., Klein, A. & Roth-Nebelsick, A. 2016. Computational fluid dynamics analysis of the fossil crinoid *Encrinus liliiformis* (Echinodermata: Crinoidea). *PLoS ONE* 11:5, e0156408. https://doi.org/10.1371/journal.pone.0156408.

Esteve, J., Gutiérrez-Marco, J.C., Rubio, P. & Rábano, I. 2018. Evolution of trilobite enrolment during the Great Ordovician Biodiversification Event: insights from kinematic modelling. *Lethaia* 51:2, 207–217. https://doi.org/10.1111/let.12242.

Esteve, J., López, M., Ramírez, C.-G. & Gómez, I. 2021. Fluid dynamic simulation suggests hopping locomotion in the Ordovician trilobite *Placoparia*. *Journal of Theoretical Biology* 531, 110916. https://doi.org/10.1016/j.jtbi.2021.110916.

Esteve, J. & López-Pachón, M. 2023. Swimming and feeding in the Ordovician trilobite *Microparia speciosa* shed light on the early history of nektonic life habits. *Palaeogeography, Palaeoclimatology, Palaeoecology* 625, 111691. https://doi.org/10.1016/j.palaeo.2023.111691.

Fortey, R.A. 1985. Pelagic trilobites as an example of deducing the life habits of extinct arthropods. *Earth and Environmental Science Transactions of the Royal Society of Edinburgh: Earth Sciences* 76:2–3, 219–230. https://doi.org/10.1017/S0263593300010452.

Gibson, B.M., Furbish, D.J., Rahman, I.A., Schmeeckle, M.W., Laflamme, M. & Darroch, S.A.F. 2020. Ancient life and moving fluids. *Biological Reviews* 96:1, 129–152. https://doi.org/10.1111/brv.12649.

Gibson, B.M., Chipman, M., Attanasio, P., Qureshi, Z., Darroch, S.A.F., Rahman, I.A. & Laflamme, M. 2023. Reconstructing the feeding ecology of Cambrian sponge reefs: the case for active suspension feeding in Archaeocyatha. *Royal Society Open Science* 10:11. https://doi.org/10.1098/rsos.230766.

Goossens, W.R.A. 2019. Review of the empirical correlations for the drag coefficient of rigid spheres. *Powder Technology* 352, 350–359. https://doi.org/10.1016/j.powtec.2019.04.075.

Gutarra, S. & Rahman, I.A. 2022. The locomotion of extinct secondarily aquatic tetrapods. *Biological Reviews* 97, 67–98. https://doi.org/10.1111/brv.12790.

Hebdon, N., Ritterbush, K.A. & Choi, Y. 2020. Computational fluid dynamics modeling of fossil ammonoid shells. *Palaeontologia Electronica* 23:1, a21. https://doi.org/10.26879/956.

Hesselbo, S.P. 1987. The Biostratinomy of *Dikelocephalus* Sclerites: Implications for the Use of Trilobite Attitude Data. *Palaios* 2:6, 605–608. https://doi.org/10.2307/3514497.

Hou, J.-B., Hughes, N.C., Hopkins, M.J. & Shu, D. 2023. Gill function in an early arthropod and the widespread adoption of the countercurrent exchange mechanism. *Royal Society Open Science* 10:8, 230341. https://doi.org/10.1098/rsos.230341.

Jacobs, D.K., Landman, N.H. & Chamberlain, J.A. 1994. Ammonite shell shape covaries with facies and hydrodynamics: iterative evolution as a response to changes in basinal environment. *Geology* 22:10, 905–908. http://dx.doi.org/10.1130/0091-7613(1994)022%3C0905:ASSCWF%3E2.3.CO;2.

Kurose, R. & Komori, S. 1999. Drag and lift forces on a rotating sphere in a linear shear flow. *Journal of Fluid Mechanics* 384, 183–206. https://doi.org/10.1017/S0022112099004164.

Lask, P.B. 1993. The hydrodynamic behavior of sclerites from the trilobite *Flexicalymene meeki*. *Palaios* 8:3, 219–225.

Lee, H. & Balachandar, S. 2010. Drag and lift forces on a spherical particle moving on a wall in a shear flow at finite *Re. Journal of Fluid Mechanics* 657, 89–125. https://doi.org/10.1017/S0022112010001382.

Li, Y. & Nielsen, P.V. 2011. CFD and ventilation research. *Indoor Air* 21:6, 442–453. https://doi.org/10.1111/j.1600-0668.2011.00723.x.

Li, Y.-H., Zhou, Z.-P., Zhai, D.-Y., O'Flynn, R.J.O., Tang, J., Xu, J.-W., Zhou, X.G. & Liu, Y. 2022. Hydrodynamics and sliding posture analysis of the Cambrian arthropod *Ercaicunia multinodosa*. *Palaeoworld* online access. https://doi.org/10.1016/j.palwor.2022.09.005.

Liu, P., Zhang, Y., Yang, X., Wang, B., Zhang, T., Sun, J., Tang, Q., He, K., Hao, W., Yue, N., He, X. & Han, J. 2022. Hydrodynamic simulations of millimeter-scale Cambrian sedentary medusozoans. *Journal of Geophysical Research* 127:10, e2022JG006854. https://doi.org/10.1029/2022JG006854.

Miller, J. 1972. Aspects of the biology and palaeoecology of trilobites. University of Manchester thesis. https://www.proquest.com/docview/2351044031?pq-origsite=gscholar&fromopenview=true&sourcetype=Dissertations%20&%20Theses.

Palmer, C. 2011. Flight in slow motion: aerodynamics of the pterosaur wing. *Proceedings of the Royal Society B* 278:1713. https://doi.org/10.1098/rspb.2010.2179.

Pates, S., Daley, A.C., Legg, D.A. & Rahman, I.A. 2021. Vertically migrating *Isoxys* and the early Cambrian biological pump. *Proceedings of the Royal Society B* 288, 20210464.

https://doi.org/10.1098/rspb.2021.0464.Pates, S. & Drage, H.B. 2024. Hydrodynamic function of genal prolongations in trinucleimorph trilobites revealed by computational fluid dynamics. *BioRxiv preprint*.

Pates, S., Ma, J., Wu, Y. & Fu, D. 2024. Impact of ontogeny and spines on the hydrodynamic performance of the Cambrian arthropod Isoxys. *Royal Society Open Science* 11:12, 240894. https://doi.org/10.1098/rsos.240894.

Pates, S. & Xue, Y. 2024. Hydrodynamic performance of Ordovician archaeostracan carapaces. *PLoS ONE* 19:5, e0304559. https://doi.org/10.1371/journal.pone.0304559.

Pearson, K. 2017. Experimental biomechanics of trinucleid fringe pits (Trilobita). Honors Papers 184, Oberlin. https://digitalcommons.oberlin.edu/honors/184.

Plotnick, R.E. & Baumiller, T.K. 1988. The pterygotid telson as a biological rudder. *Lethaia* 21:1, 13–27. https://doi.org/10.1111/j.1502-3931.1988.tb01746.x.

Rahman, I.A. 2017. Computational fluid dynamics as a tool for testing functional and ecological hypotheses in fossil taxa. *Palaeontology* 60:4, 451–459. https://doi.org/10.1111/pala.12295.

Rahman, I.A. 2020. Computational fluid dynamics and its applications in echinoderm palaeobiology. *Elements of Paleontology*. Cambridge University Press. https://doi.org/10.1017/9781108893473.

Rahman, I.A. & Lautenschlager, S. 2016. Applications of three-dimensional box modeling to paleontological functional analysis. *The Paleontological Society Papers* 22, 119–132. https://doi.org/10.1017/scs.2017.11.

Rahman, I.A., Zamora, S., Falkingham, P.L. & Phillips, J.C. 2015. Cambrian cinctan echinoderms shed light on feeding in the ancestral deuterostome. *Proceedings of the Royal Society B* 282, 20151964. http://dx.doi.org/10.1098/rspb.2015.1964.

Rahman, I.A., O'Shea, J., Lautenschlager, S. & Zamora, S. 2020. Potential evolutionary trade-off between feeding and stability in Cambrian cinctan echinoderms. *Palaeontology* 63:5, 689–701. https://doi.org/10.1111/pala.12495.

Rauen, W.B., Lin, B., Falconer, R.A. & Teixeira, E.C. 2008. CFD and experimental model studies for water disinfection tanks with low Reynolds number flows. *Chemical Engineering Journal* 137:3, 550–560. https://doi.org/10.1016/j.cej.2007.05.011.

Rohatgi, A. 2025. WebPlotDigitizer v.5.2. https://automeris.io.

Shi, P. & Rzehak, R. 2019. Lift forces on solid spherical particles in unbounded flows. *Chemical Engineering Science* 208: 115145. https://doi.org/10.1016/j.ces.2019.08.003.

Shi, P. & Rzehak, R. 2020. Lift forces on solid spherical particles in wall-bounded flows. *Chemical Engineering Science* 211: 115264. https://doi.org/10.1016/j.ces.2019.115264.

Song, H., Song, H., Rahman, I.A. & Chu, D. 2021. Computational fluid dynamics confirms drag reduction associated with trilobite queuing behaviour. *Palaeontology* 64:5, 597–608. https://doi.org/10.1111/pala.12562.

Trenchard, H., Brett, C.E. and Perc, M., 2017. Trilobite 'pelotons': possible hydrodynamic drag effects between leading and following trilobites in trilobite queues. *Palaeontology* 60:4, 557–569. https://doi.org/10.1111/pala.12301.